Available online at www.sciencedirect.com
ScienceDirect
Journal of Nuclear Materials 367–370 (2007) 399–410
journal of nuclear materials
www.elsevier.com/locate/jnucmat

The transport and fate of helium in nanostructured ferritic alloys at fusion relevant He/dpa ratios and dpa rates

T. Yamamoto [a,*], G.R. Odette [a], P. Miao [a], D.T. Hoelzer [b], J. Bentley [b], N. Hashimoto [b], H. Tanigawa [c], R.J. Kurtz [d]

[a] Department of Mechanical Engineering, University of California Santa Barbara, Santa Barbara, CA 93106-5080, USA
[b] Oak Ridge National Laboratory, Oak Ridge, TN 37831, USA
[c] Japan Atomic Energy Agency, Tokai-mura, Naka-gun, Ibaraki 319-1195, Japan
[d] Pacific Northwest National Laboratory, MS P8-15, P.O. Box 999, Richland, WA 99352, USA

Abstract

A novel in situ $^{59}Ni(n,\alpha)$ reaction He-implanter technique is described, that can be used to characterize the effect of the He/dpa ratio on microstructural evolution and changes in the flow properties of various materials at fusion relevant conditions. Irradiations in the high flux isotope reactor resulted in α-implantation from 1 to 5 μm thick NiAl coatings on TEM discs producing a uniform He concentration of 5–50 appm He/dpa to a depth of 5–8 μm. Initial post-irradiation TEM observations of MA957 irradiated to 9 dpa and 380 appm He at 500 °C provide strong evidence for the existence of a high density of small $\leqslant$1 nm size bubbles trapped on nano-scale YTiO clusters. In contrast, similar irradiations of Eurofer 97, described in a companion paper, produce a lower number density of larger cavities, which may be a mixture of bubbles and voids.

1. Introduction

Predicting and mitigating the effects of a combination of high levels of transmutant He and displacement damage (dpa) produced by high-energy neutrons on the mechanical properties of structural materials is one of the key challenges in the development of fusion energy. Fundamental issues about He–dpa synergisms include: the basic interacting mechanisms controlling He and defect transport, fate and consequences and how are they influenced by the starting microstructure and irradiation variables (dpa rate, He/dpa ratio, temperature and applied stress); and how can the detrimental effects of He–dpa synergisms be mitigated and managed by proper microstructural design?

Understanding the effects of He–dpa synergisms on microstructural evolution and property changes under fusion relevant conditions (He/dpa $\approx$ 10 appm/dpa, $\approx 10^{-6}$ dpa/s) is the primary motivation for proposals to construct a high-energy fusion neutron source, such as the IFMIF [1]. However, in the meantime, it will be necessary to utilize fission reactor and dual ion irradiations to study He–dpa synergisms. Dual ion irradiations are useful to explore mechanisms, but they do not simulate fusion conditions because of their highly accelerated

* Corresponding author. Tel.: +1 805 893 3848; fax: +1 805 893 4731.
E-mail address: yamataku@engineering.ucsb.edu (T. Yamamoto).

0022-3115/$ - see front matter © 2007 Elsevier B.V. All rights reserved.
doi:10.1016/j.jnucmat.2007.03.047

dpa rates and other confounding factors, such as the proximity of free surface sinks. To date, most fission reactor studies of He–dpa synergisms have utilized ^{59}Ni and ^{10}B (n,α) 'alloying element' reactions to produce high levels of He [2]. However, with the exception of austenitic stainless steels, neither Ni nor B constitute a normal alloying element in candidate fusion structural material systems [≈ 8Cr tempered martensitic steels (TMS), nano-dispersion strengthened ferritic alloys (NFA), solid solution vanadium alloys and SiC/SiC ceramic composites]. Thus while Ni or B doping, combined with isotopic and/or spectral tailoring, are very useful, these techniques cannot be considered simulations either, since they all introduce a significant number of confounding factors. It is also noted, however, that spallation proton and mixed proton–neutron irradiations produce very high levels of He at rates of up to ≈ 80–150 appm/dpa [2–4].

In situ He implantation in fission reactors is an alternative and very attractive approach to assessing the effects of He–dpa synergisms that avoids most of the confounding effects of doping. The basic idea is to use an implanter foil to inject high-energy α-particles into an adjacent sample simultaneously undergoing neutron induced displacement damage. Implanting He using the decay of an α-emitting radioactive isotope adjacent to the target specimen was first proposed in the late 1970s to early 1980s [5,6]. However, the isotope decay technique produces few dpa and a very high He/dpa ratio. The in situ nuclear-reaction implanter technique was first proposed by Odette, who specifically suggested utilizing (n,α) reactions from triple fission [7]. The ≈ 16 MeV triple fission α-particles emanating from a thick ^{233}U containing layer can uniformly implant a thin Fe specimen up to ≈ 60 μm thick at fusion relevant He/dpa ratios [7]. This dimension is sufficient for specialized tensile specimen tests, possibly even in the creep regime. Further, while the dimensions are far too small for measuring fracture toughness, they may be sufficient to assess fast fracture related processes and mechanisms, such as the weakening of grain boundaries due to He accumulation. The triple fission technique was applied to a tensile specimen of a ferritic steel [8]. However, this experiment was not completely successful due to difficulties in controlling temperature increases arising from heat generated by the fission reaction, as well as in obtaining the desired He/dpa ratio.

Mansur and Coghlan first proposed using thin Ni containing implanter foils, specifically based on the ^{59}Ni(n_{th},α) reaction [9]. In this case a uniform deposition region is produced over the range of the α-particle (up to ≈ 8 μm, see below) in the implanter foil and thick specimen [9].

Unfortunately, these in situ implanter ideas lay dormant for many years, but they were resurrected by our group at UCSB in the early part of planning for a series of high flux isotope reactor (HFIR) experiments that form the core of the ongoing US-JAERI (currently JAEA) fusion materials collaboration. After considering various alternatives, we implemented the thin Ni foil approach [9], which is much simpler than the method proposed in Reference [7]. A thin μm-scale Ni containing coating on TEM discs implants He uniformly to a depth of ≈ 5–8 μm. This is sufficiently thick for low load Vickers micro-hardness and nano-hardness measurements, as well as for extensive microstructural characterization. Hence, the objective of the initial phase of this research was to design, develop and implement a technique to deposit and characterize Ni containing implanter coatings on TEM discs to be included in coated–uncoated pairs in the HFIR-PTP irradiations, with nominal peak target doses of 10, 25, and 60 dpa at irradiation temperatures of 300, 400 and 500 °C. The initial results of the implanter experiments on MA957 are reported here.

2. Implanter layer design concepts

There are at least three basic approaches to implanter *layer* design. Here we will refer to *thin* and *thick*, specifically meaning a specimen (t_s) or implanter layer (t_f) thickness that is less than or greater than the corresponding α-particle range, respectively. Thin layers produce uniform implantation to a certain fraction of the α-particle range at a selected implanter layer thickness-dependent He/dpa ratio. Thick implanter layers on one side of a thick specimen produce linear concentration profiles, with the maximum concentration of He at the specimen surface. Thick implanter layers on both sides of a thin specimen also produce a uniform concentration profile at the maximum concentration of He. In this section, the conceptual design of a thin implanter layer is first summarized, followed by a description of the actual fabrication and characterization of NiAl coatings on TEM discs to attain controlled fusion relevant He/dpa ratios in the JP26 to JP28/29 experiments.

2.1. He implantation profiles

Packan and Coghlan [5] first derived rigorous expressions for implantation profiles from thick and thin alpha decay emitter layers, that was later elaborated by Garner [6]. We summarize only important results and a simpler mathematical approach for purposes of illustration. The implanter layer contains an isotope with a large (n,α) reaction cross-section, such as ^{59}Ni, ^{10}B, or ^{6}Li, producing an α-particle with characteristic energy and corresponding range in the implanter layer and sample of R_f and R_s, respectively. Fig. 1(a) shows thick specimen, thick implanter layer configuration. The α-particles emitted from the layer under neutron irradiation are deposited in the specimen up to the depth of R_s. All calculations in this section assume the area (y,z) dimensions of the implanter layer-specimen are much larger than R_f, hence, edge effects can be neglected. For simplicity, we assume $R_f = R_s = R$ and ignore α-particle straggling. The He concentration, C_{He}, at a depth x ($x < R$) in the specimen is proportional to the area fraction, $f(x)$, of the spherical shell in the implanter layer of radius, R, centered on x, as shown in Fig. 1(b). The $f(x)$ is given by

$$f(x) = \int_0^{\theta_{max}} 2\pi R \sin\theta \cdot R d\theta / 4\pi R^2 = \frac{1}{2}\left(1 - \frac{x}{R}\right). \quad (1)$$

Here θ is the angle between the radial vector **R** and the normal to the specimen surface and θ_{max} occurs at the implanter layer/specimen boundary. The resulting He concentration profile is linear, with $f(x)$ decreasing from 1/2 at $x = 0$ to 0 at $x = R_s$ as shown in Fig. 1(c). Differences in the implanter layer versus specimen α-particle ranges, R_f and R_s, are accounted for by a range ratio factor of R_f/R_s, and $C_{He}(x)$ is

$$C_{He}(x) = \frac{C_f}{2}\frac{R_f}{R_s}\left(1 - \frac{x}{R_s}\right). \quad (2)$$

Here C_f is the volumetric concentration of He in the implanter layer which is the same as the bulk concentration for a given implanter layer composition and neutron dose. The corresponding molar (or atomic) concentration C_f must be adjusted by multiplying C_f by the ratio of the layer/specimen atomic densities (N), N_f/N_s.

The gradient in the He concentration may be acceptable, or even advantageous, in some cases. However, in other cases a uniform He distribution

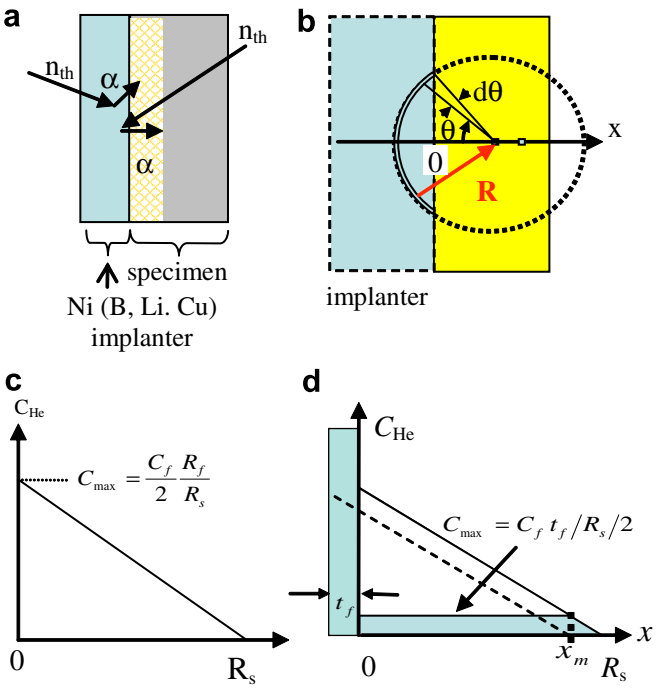

Fig. 1. Schematic illustration of: (a) a thick implanter foil; (b) the implanter source volume for He deposited at a depth x in the specimen; (c) the He concentration profile for thick foil implantations and (d) the uniform He concentration profile for thin foil.

is preferable. Regions with uniform concentrations can be obtained using thin specimens implanted from both sides [7]. However there are practical difficulties in fabricating such thin specimens. Fortunately, as illustrated in Fig. 1(d), a uniform distribution of He near the surface of a thick specimen can also be obtained by using thin implanter layers, with $t_f \ll R$ [5,6,8]. The He profile for a thin implanter can be determined by simply superimposing linear profiles from various depths in the layer, then subtracting off the *missing* contributions from the (n,α) reactions further from the interface. For $R_f = R_s = R$, the result is a uniform region of He concentration of $C_{He}(x) = [C_f/2][t_f/R]$ up to a maximum $x_m = R - t_f$. At larger $x > R - t_f$ the $C_{He}(x)$ decreases from $[C_f/2][t_f/R]$ to 0 at $x = R$. In the case where $R_f \neq R_s$ the $x_m = R_s(1 - t_f/R_f)$. Thus

$$C_{He}(x) = \frac{C_f}{2}\frac{t_f}{R_s} \quad (0 \leqslant x \leqslant x_m) \quad \text{or}$$
$$\frac{C_f}{2}\frac{R_f}{R_s}\left(1 - \frac{x}{R_s}\right) \quad (x_m < x < R_s). \tag{3}$$

The key conclusions from this analysis are:

1. Various He profiles in a specimen can be produced with combinations of one or two-sided, thick or thin implanter layer and specimen.
2. Uniform helium concentrations can be produced over useful regions of a specimen by thin layer implantation from one side [9].
3. The concentration of He in a specimen can be controlled by both the thickness and composition (coupled with the neutron spectrum) of a thin implanter layer. Thus it is possible to control (dial-in) the corresponding He/dpa ratio over a wide range of values [9].
4. Thin layer implantation from two sides of a thin specimen roughly doubles the size of the region with a uniform He concentration.

3. Irradiation experiments and post-irradiation characterizations

3.1. He implanter foil design for iron based alloys irradiated in the HFIR PTP JP26 to 28/29 experiments

The ^{59}Ni isotope is an obvious leading candidate (n,α) reaction source, yielding a 4.79 MeV α-particle. Since ^{59}Ni is radioactive, with a half life of $t_{1/2} = 7.5 \times 10^4$ y, the simplest approach is to breed it in situ, based on the reaction sequence ^{58}Ni(n_{th},γ)^{59}Ni(n_{th},α). The time-dependent concentration of ^{59}Ni(n_{th},α), hence, the He generation rate in the implanter layer, depends on the pertinent spectral averaged ^{58}Ni(n_{th},γ), ^{59}Ni(n_{th},α) and total ^{59}Ni n-capture, ^{59}Ni(n_{th}, tot.), cross-sections. The total dpa is also determined by the corresponding spectral averaged dpa cross-section. The pertinent cross-sections were used to compute He concentration, C_f (appm), for pure Ni versus dpa for irradiations in the HFIR PTP spectrum [10].

We chose to use NiAl rather than pure Ni for a number of reasons including: (a) NiAl is believed to be more stable under irradiation than pure Ni or Ni alloys, since they would have the tendency to swell; (b) NiAl has a coefficient of thermal expansion that is similar to that of ferritic steels; (c) it is relatively easy to co-deposit Ni and Al over the wide range of stable composition of single-phase NiAl, from 46 to 59 at.%. The basic implanter coating design used 5.9 and 7.9 g/cm^3 for the densities of NiAl and ferritic steels, respectively, and the corresponding α-particle ranges of 11.5 and 9.1 μm calculated using TRIM 2002 code as the average for 10 000 4.76 MeV He ions.

Figs. 2(a) and (b) show the He concentration profiles in ferritic steel specimens for NiAl implanter coating with $t_f = 1$, 2 and 4 μm for low (4.3 dpa) and high (60 dpa) dose conditions, corresponding to target exposures for the JP-26 and JP-28/29 capsules, respectively. Fig. 2(c) shows the He/dpa ratio produced by a 2 μm thick NiAl coating as a function of dpa. Due to the dose transient to 'burn-in' of ^{59}Ni to a quasi steady-state concentration, producing an approximately constant He generation rate, the He/dpa ratio rapidly increases during the first 10 dpa, followed by just a slight increase and ultimately a slow decrease, thereafter. In the JP26 capsule receiving dpa ranging from about 4 to 10 dpa, the He/dpa ratio roughly doubles in going from the lowest to highest dose location. Note, pre-bred ^{59}Ni coatings could be used to avoid the He generation transient.

Thus, implanter coating designs targeting a specified He/dpa ratio must consider the intended dpa dose. Implanter coating thicknesses of 1, 2 and 4 μm yield He/dpa ratios of ≈ 5, 10 and 20 appm He/dpa at the target dose of 4.3 dpa for the 300 and 400 °C zones in JP26 capsule. As shown in Figs. 2(a) and (b), there is a direct trade-off between the implanter coating thickness, and the corresponding region of uniform He composition in the specimen,

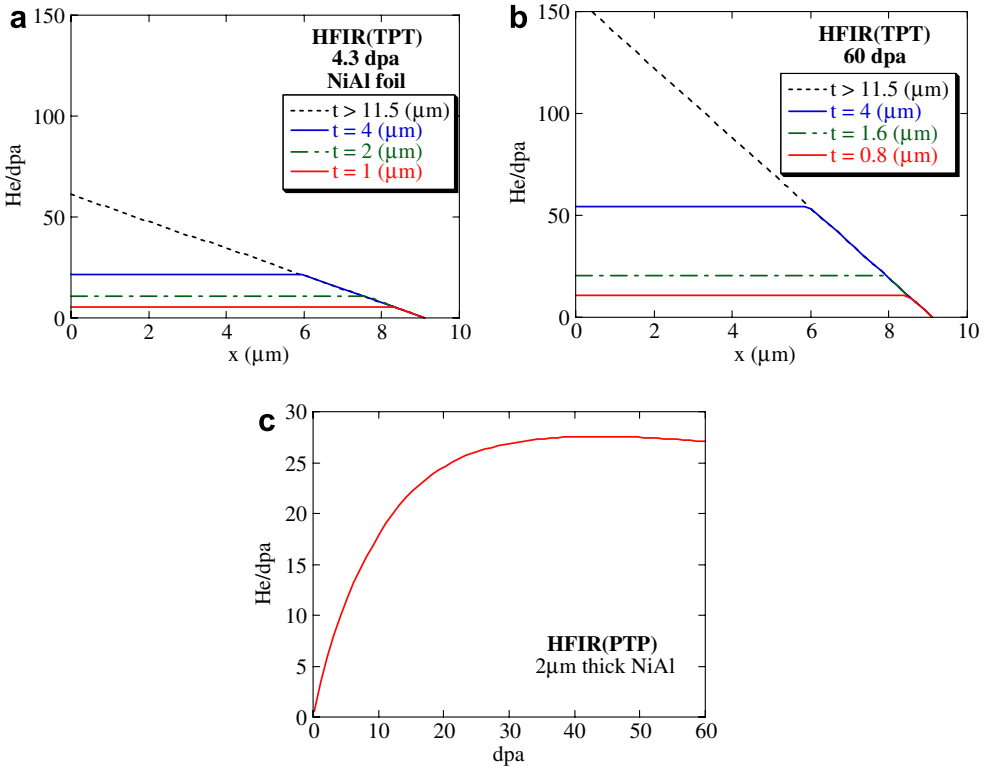

Fig. 2. He concentration profiles in ferritic steel specimens for (a) low (4.3 dpa) and (b) high (60 dpa) dose conditions, respectively, for NiAl implanter foils with $t_f = 1$, 2 and 4 μm; and, (c) He/dpa ratio produced by 2 μm NiAl coating as a function of dpa.

and the maximum He/dpa ratio that can be achieved. However, even at the lowest dose irradiation, an average He/dpa ratio of 20 appm He/dpa can be attained over ≈ 6 μm. Rather than trying to make thinner coatings, which are more difficult to characterize, similar thicknesses were used for the irradiations to 10 dpa in the JP26 at 500 °C capsule and for all the JP27 and JP28/29 capsules. The two thinner coatings yield nominal He/dpa of 10 and 20 appm, while as shown in Table 1, they range from 38 to 65 appm/dpa for the thickest coatings. Maximum He levels in the JP27 and JP28/29 capsules will range from 570 to 2770 appm at the target doses, enabling exploration of He effects at levels comparable to, or in excess of, conditions where severe degradation of mechanical properties have been observed in spallation proton irradiations and He ion implantation experiments [2–4].

3.2. Implanter coating fabrication and characterization

Thin 0.8–5 μm NiAl implanter layers were deposited on TEM disc specimens. The TEM disc surfaces were first polished on both sides. The deposition side was finished to 0.05 μm alumina to ensure the dense growth of the NiAl deposit, while the other side was finished to 1200 grit paper, or better, to maintain good heat transfer for substrate temperature control during deposition. Ni and Al were co-deposited using an electron beam (EB) physical vapor deposition (PVD) system. The deposition rates of each element were independently monitored with a calibrated crystal oscillator mass monitor. The EB currents were adjusted and controlled to maintain the desired ≈ 1/1 Ni/Al atomic ratio in the deposit. The TEM disc substrate temperature was held at 500 °C during deposition. The co-deposited film was grown at a typical rate of ≈ 1 μm/h.

Careful characterization of the implanter foil coating was an extremely important part of this work, especially during the stage of developing and calibrating the deposition procedure. The characterization included the following procedures:

- The primary technique to *non-destructively* characterize the effective thickness of the coatings was based on pre and post-deposition precision

weighing of the thin substrate monitors, as well as essentially all of the TEM discs. Reasonable weight-thickness relation was confirmed by additional cross-sectional thickness measurement on selected coatings. However, the latter was not the primary coating characterization method since it creates half discs that are hard to load and with poor heat transfer characteristics. The overall thickness uncertainties of the weighing technique are estimated to be $\approx \pm 0.1$ μm.

- Cross-sections of the discs-coatings system were examined in the SEM to characterize the adherence of the coating and any defects present. The coatings were generally found to be well bonded and defect free.
- The coatings were also selectively micro-machined and imaged in the focused ion beam (FIB) system for similar reasons.
- SEM EDX spectra measurements were used to evaluate the composition of the deposits, which generally ranged from 48 to 55 at.% Ni. Calibration of the Fe signal as a function of the NiAl thickness was also used to help verify the coating thickness. SEM EDX was used to examine essentially 100% of the coated TEM discs used in the irradiations.
- XRD was selectively used to verify the presence of a single-phase NiAl.
- AFM was selectively used to characterize the uniformity and roughness of the coating.

To summarize, the results of the various characterization techniques of the coatings, the FIB cross-sectioning showed that dense implanter coating had grown continuously from the substrate surface to the target thickness. The XRD showed that the deposited layer consisted of single-phase NiAl. The surface roughness measured by AFM was typically $\leqslant 0.04$ μm, reflecting the substrate roughness. Overall, the roughness and coating thickness variations are expected to contribute spatial differences in the He concentration that are less than ±4%. Along with crystallographic information from XRD, the EDX analyses confirmed that the Ni content was within the range of NiAl phase. All discs were subsequently optically inspected to verify that they remained damage free. A total of approximately 400 coated discs were fabricated and characterized as described above, and a subset of about 300 of them that best achieved a high quality implanter foil coating were selected for subsequent irradiations. The coated discs were paired with highly polished uncoated discs in order to produce similar He/dpa ratios in the latter.

3.3. Specimen matrix

The He implantation technique was applied to three types of materials: cold-worked and annealed unalloyed Fe, ≈ 8Cr tempered martensitic steels (TMS), and nano-dispersion strengthened ferritic alloys (NFA). Table 1 summarizes the details of the total ≈ 180 He injected TEM discs that are included in the 500 °C irradiation matrix. Essentially identical sets of discs are included in the 300 and 400 °C matrices. Of course, unimplanted TEM specimens of all the materials are included in the matrix to provide a low He/dpa (<1 appm He/dpa) baseline data for the effects of higher He. Further, the matrix includes some Ni-doped model alloys as an alternative means of introducing He.

It is notable that the enormous range of microstructures covered by these three types of materials not only provides an unprecedented opportunity to better understand key damage and processes, but will also yield a database to guide the design of new and improved alloy systems. For example, the behavior and effects of He in the cold-worked and annealed Fe will provide clear, single-variable-type insight on the effects of dislocation structures on the transport and fate of He. The NFA in the specimen matrix include a series of model materials produced by UCSB (the U14-series) and ORNL (the O14 alloy). The U14YWT and U14WT variants include HIPing at 850, 1000 and 1150 °C resulting in a wide range of fine-scale precipitate structures, with large differences in their sizes, number densities (hence, sink strengths) and basic structures (thus, different interface characteristics) ranging from non-equilibrium coherent Y–Ti–O clusters to semi-coherent, pyroclore-type and other oxide phases [11–13]. The specimen matrix also includes the commercial, or semi-commercial, alloys: MA957, Japanese 12WYT and PM2000 alloys. Note, depending on the alloy and processing path, the NFA also represent a wide range of dislocation and grain structures as well.

The TMS in the matrix include 3 variants of F82H, including one with 20% cold work, and Eurofer 97. The basic microstructure of the TMS consists of: (a) μm-scale laths arranged in small $\leqslant 10$ μm lath packets that are contained in larger 20–80 μm prior austenite grains; (b) medium-to-coarse scale Cr-rich carbides; and, (c) medium-to-

Table 1
Summary of the TEM specimens for the JP26, JP27 and JP28/29 capsules along with the designed NiAl coating thicknesses and expected dose and He/dpa

	JP-26			JP-27			JP-28/29		
$T_i = 300$ °C									
dpa	4.3			11			21		
He/dpa (appm)	5	11	21	10	20	50	10	21	52
$T_i = 400$ °C									
dpa	4.3			11			45		
He/dpa (appm)	5	11	21	10	20	50	11	22	55
$T_i = 500$ °C									
dpa	10			25			50		
He/dpa (appm)	9	19	38	13	26	65	11	22	55
NiAl coating thickness (μm)	1	2	4	1	2	5	0.8	1.6	4
Material									
Fe	1	2	1	2	1	1	1	2	1
Fe+20%CW	2	2	2	2	2	2	2	2	2
F82H IEA	2	2	2	2	2	2	2	2	2
F82H-mod.3	2	2	2	2	2	2	2	2	2
F82H-mod.3+20%CW	2	2	2	2	2	2	2	2	2
Eurofer 97	2	**2**	**2**	2	2	2	2	3	2
U14YWT850			3			3		1	3
U14YWT1150			3			3			3
U14YW1150			3			3			3
O14YWT850			3			3			3
U14WT1000			2						
U14WT1150						2			2
MA957 (US)			2			2	1		2
MA957 (F)			2			2			2
12YWT	2	2	2		1	2	2	2	2
PM2000			2	2	1	2			2
Total	13	14	33	14	13	33	14	16	33

Specimen counts are for 500 °C subcapsules just as representative.

high (the cold-worked alloy) dislocation densities. The TMS microstructures also provide many trapping sites for He, but recent evidence suggests that He accumulation at prior austenite grain boundaries may still lead to a severe non-hardening embrittlement and intergranular fast fracture at lower irradiation temperatures ($\leqslant\approx$ 350 °C) and that these microstructures are unstable at higher irradiation temperatures (>450 °C) [2–4,14].

3.4. Post-irradiation characterization studies

Various types of TEM techniques have or will be used as the primary tool for post-irradiation characterization of the implanted layers. The 5–8 μm thick region is made readily accessible by a variety of well-developed sample preparation techniques, including: back thinning, cross-sectioning and precision dimpling and FIB micromachining. The TEM studies will focus on: (a) the fate of helium; (b) the effect of the He/dpa ratio on the overall microstructural evolution; (c) the effects of synergistic interactions between the He/dpa ratio and other irradiation variables such as dpa, temperature, as well as the metallurgical variables (the starting microstructure and microchemistry) on He fate and microstructural evolution and (d) the ability of nano-scale precipitates and dislocations to trap and disperse (manage) He in fine-scale bubbles. The He contents of the layers have and will be assessed by isotope-dilution gas mass spectrometry following vaporization in a resistance-heated graphite crucible in the mass spectrometer vacuum furnace [15].

Both nano-hardness and low load micro-hardness have and will also be used to characterize the effects of He/dpa ratio on irradiation hardening (or softening) processes. Nano-hardness can be used

to indent across a cross-section of the implanted layer directly, while low load micro-hardness is carried out on the implanter surface (requiring removal of the NiAl on coated disks). While fracture tests of the implanted specimens are not possible per se, disk bend tests at low temperatures can be used to probe phenomena such as intergranular fracture on He weakened boundaries. Other potential characterization techniques include X-ray scattering, positron annihilation spectroscopy and He desorption spectroscopy.

4. Preliminary results

The first series of TEM studies have been performed on MA957 and Eurofer 97 [15] specimens irradiated in the JP26 capsule. The NFA MA957, which is the focus of this paper, was irradiated to $\approx$ 10 dpa at 500 °C, with an implanted layer containing $\approx$ 380 appm He. Electron transparent 10×20 μm sections were FIBed out of a half TEM disc from the $\approx$ 6 μm thick implanted region at the Japanese Atomic Energy Agency. The specimen surfaces were then milled with low-energy Ar^+ ions to remove surface layer damage and sent to Oak Ridge National Laboratory for microstructural observations.

The initial TEM has involved use of two techniques carried out on a LaB6 Phillips CM30 instrument. A standard through focus series imaging was used to assess small features that produce fringe images that change from white to black in going from over to under focus conditions, respectively, as is characteristic of voids or bubbles. Figs. 3(a) and (b) show a set of through focus images taken at about 6 μm from the NiAl deposited surface indicating the presence of many such features. Unfortunately, in this case, the detection of both NF and bubbles was complicated by surface oxide contamination, which produces very similar images. The most conclusive result is that larger bubbles, of the type observed in Eurofer 97 as shown in Fig. 3(e), at the same irradiation condition, were not found in the implanted region of MA957. The deduction is that the He must be located in bubbles, which range from atomic dimensions up to less than $\approx$ 1.5 nm.

A second technique, Energy Filtered TEM (EFTEM) with a Gatan imaging filter, was used to assess the NFs themselves. EFTEM produces elemental maps of the alloy constituents and compositional discontinuities produce light or dark regions, quantified in terms of so-called atomic jump ratios, corresponding to higher (e.g., Ti) or lower (e.g., Fe) concentrations associated with the presence of a NF and/or bubbles. Figs. 3(c) and (d) show EFTEM maps of Fe (Fig. 3(c)) and Ti (Fig. 3(d)), respectively. Nearly all the black spots ($\approx$ 95%) in Fig. 3(c) showing a depletion in Fe correspond to either a clear white spot or a light diffuse cloud in Fig. 3(d) showing enrichment in Ti, clearly indicating the presence of NF, that are known to be enriched in Y, Ti and O [11–13]. The average size of the NFs is $\approx$ 3 nm, while much fewer but larger $\approx$ 9 nm scale features are also observed.

A detailed analysis of NF number density and diameter distribution analysis was performed on EFTEM image. First a black and white image map of NFs that were clearly identified in the gray-scale EFTEM images was created and area number density and size distribution were determined using a software package Image J. The foil thickness $\approx$ 18 nm in the imaged region was measured by electron energy loss spectrometry (EELS). The corresponding average NF diameter and number density were 3.1 ± 0.7 nm and 8.0×10^{23} m^{-3}, respectively. These results compare very favorably with previously reported values for unirradiated MA957 determined by small angle neutron scattering (SANS) 2.6 nm and 7×10^{23} m^{-3}, respectively [11]. These observations also show that the NFs are stable after 9 dpa irradiation at 500 °C.

A further comparison of the EFTEM and the through focus contrast images was carried out to probe possible NF-bubble associations in the 18 nm thick foil region. About 69% of the black spots in Fig. 3(a) (under focus) are also correlated with the black features observed in Fig. 3(c) (EFTEM). As illustrated in the enlarged images, in almost all cases the through focus sequence of the NF, clearly identified by EFTEM mapping, showed the presence of one or more bubbles as black–white contrast for over-under focus. The association of bubbles and somewhat larger oxide features is illustrated in the through focus images in another part of the specimen shown in Figs. 4(a)–(c). While this region is too thick for EFTEM observations, the presence of tiny bubbles on the oxide interface is evident. Further and detailed investigation is necessary to confirm the bubble association with NFs. However the fact that the preliminary quantitative analyses described below gives the bubble number density similar to that of NFs also suggests the correlation.

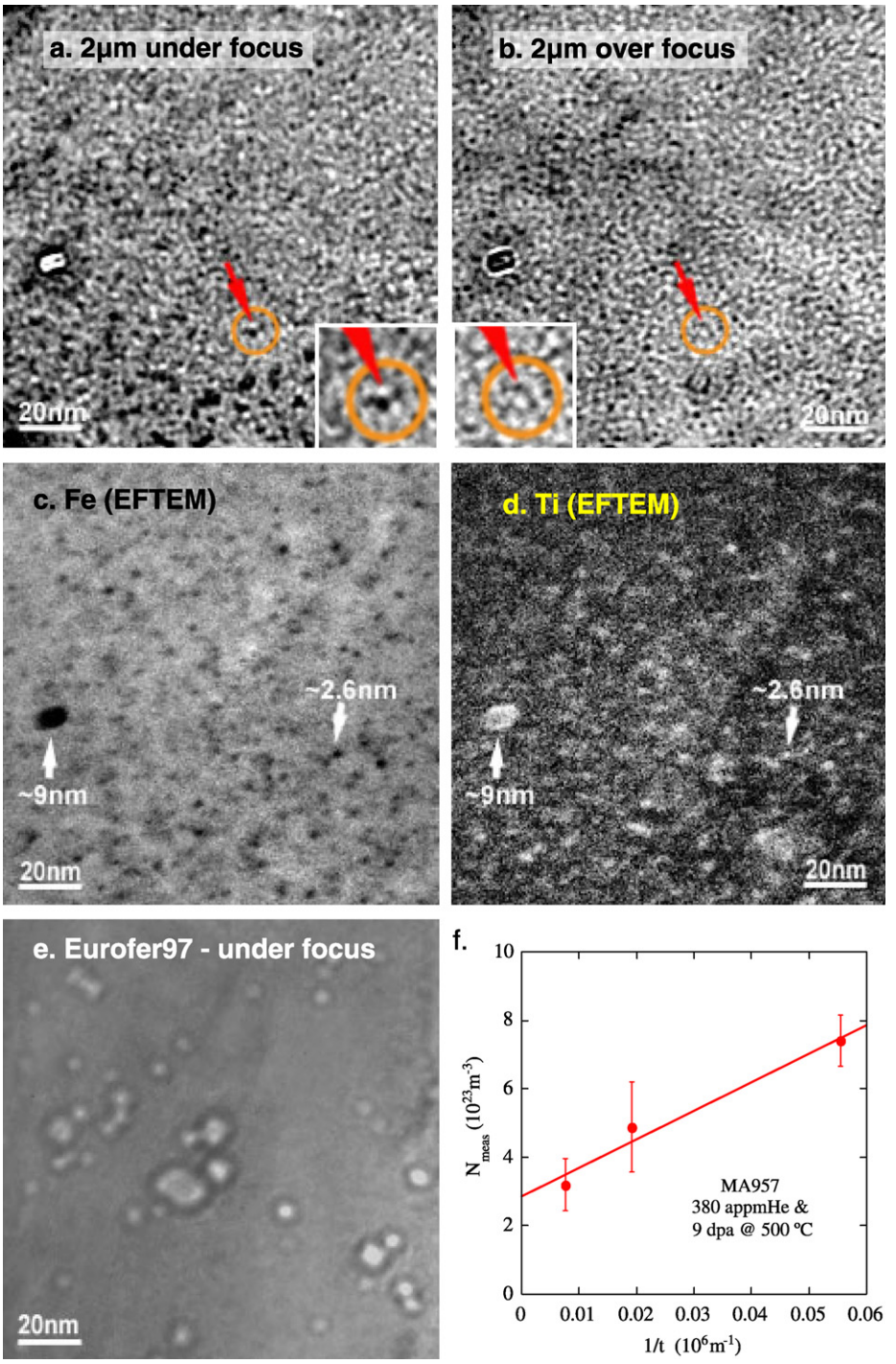

Fig. 3. TEM images of a He implanted region in MA957 for bubble contrast; (a) 2 μm under focus; (b) 2 μm over focus; (c) Fe and (d) Ti EFTEM compositional images; (e) under focus image for He implanted Eurofer 97 as a direct comparison and (f) estimated bubble number densities as a function of the inverse specimen thickness to estimate bulk He bubble number densities.

Assuming a similar EFTEM through focus NF-bubble association, a detailed image analysis was performed for three rectangular areas of 0.0226 (18 nm thick), 0.0250 (52 nm thick) and 0.00228 (131 nm thick) μm^2 at various foil thicknesses, t_l, measured by EELS or thickness fringe techniques.

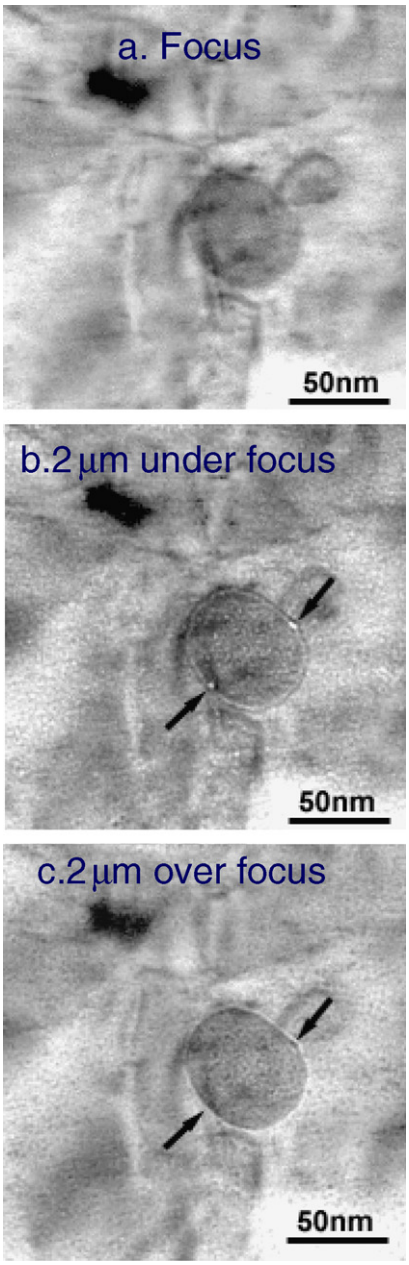

Fig. 4. Through-focus series TEM images of He implanted MA957 near an oxide particle.

The corresponding thickness-dependent volume densities of the putative bubble-features, N_b, are 7.4, 4.9 and $3.0 \times 10^{23}\,m^{-3}$, respectively. For 131 nm thick location, considering overlap in a column $\approx$ 1.6 nm in diameter, and the estimated volume fractions of $\approx$ 0.08%, yields $N_b \approx 3.2 \times 10^{23}\,m^{-3}$. Plotting the number density versus $1/t_l$ gives the bulk estimate when $1/t_l$ is extrapolated to 0, as shown in Fig. 3(f), yielding an estimated $N_b \approx 3 \times 10^{23}\,m^{-3}$. The average diameter of the bubbles in the 18 nm thick region was determined by randomly selecting 40 bubbles from the 1 μm under focus TEM image and very carefully measuring the diameters of their central white dots. The measured white dot radius was then converted to a real bubble diameter using the correction curve of Rühle and Wilkins [16]. The estimated average bubble diameter was 0.9 ± 0.3 nm.

These TEM results can be used to estimate total He contained in an average bubble, n_{He}. A high-pressure equation-of-state compressibility factor, $Z(P)$, [17] was used assuming that all bubbles are in equilibrium and that the pressure, P, in a bubble is given by

$$P = \frac{2\gamma}{\langle r \rangle} = \frac{3Zn_{He}kT}{4\pi\langle r \rangle^3}, \tag{4}$$

where γ is the surface energy, which is taken to be $\approx 2\,J/m^2$, and $\langle r \rangle$ is the mean bubble radius. The estimated total He concentration $N_b n_{He} \approx$ 130 appm is conservative based on the estimated bubble density, but reasonably consistent with the nominal implanted level of 380 appm, especially considering the various uncertainties and approximations.

It is also useful to briefly compare and contrast the results on MA957 with the observations on Eurofer 97 for irradiations under nearly identical conditions (372 appm He/9 dpa/500 °C) as well as at lower irradiation temperatures and doses [15]: 89 appm He/4 dpa/300 °C; 82 appm He/4 dpa/400 °C, 168 appm He/9 dpa/500 °C. The Eurofer 97 results can be summarized as follows:

- Thermal desorption of a thin sample nominally taken from the implanted layer measured $\approx$ 132 appm He, comparing favorably to a nominal value of 168 appm. Similar measurements on full $\approx$ 200 μm thick samples showed an overall He concentration of 12.2 appm, corresponding He concentration in the implanted layer of $\approx$ 300 appm. These results demonstrate the successful use of the implanter technique.
- Helium bubbles were found in the implanted region at all three irradiation temperatures, with estimated mean diameters of $\approx$ 0.9, 3.0, and 4.3 nm at 300, 400 and 500 °C, respectively. The corresponding bubble densities are estimated to be 3.6×10^{23}, 1.2×10^{22}, $1.5 \times 10^{22}/m^3$. An assessment of the He content of the bubbles also was in good agreement with the implanted values. At

500 °C ≈ 10 nm faceted cavities were also observed, which may be voids. The bubble density suggests a He diffusion distance at 500 °C of ≈ 20 nm.
- There is evidence that loop and void formation may have been suppressed at 300 °C by a high-density of small He bubbles serving as point defect recombination centers.
- At 400 and 500 °C pre-existing dislocations appear to be preferred He bubble nucleation sites.

In summary, the Eurofer 97 results described above show that approximately the expected amount of He is injected and collects in bubbles that form by long range He diffusion, over distances of ≈ 20 nm at 500 °C. This distance is more than ≈ 4 times the average diffusion distance of He to NF in MA957, hence, there is no physical reason to believe that diffusion is insufficient for He to reach NF trapping sites. Notably, trapping of Ar gas at the interface of NF in NFAs have been reported by Kilimiankou et al. [18]. Further, Kim et al. have reported He trapping at NF in dual ion irradiations [19]. In addition, the sink strength of the NF, which is ≈ 10^{16} m^{-2}, is much larger than that for other sites. Thus even if He is weakly trapped at the interface, presumably it will recycle between the NF many times before it is absorbed by other sinks. Further, once nucleated He bubbles themselves act as excellent sinks for additional He trapping, as well as efficient recombination centers for vacancy and self-interstitial defects. Finally, modeling studies we have carried out on He partitioning to various sinks in NFAs support the conclusion that NF efficiently trap high levels of He in the form of ultra-small bubbles, that are stable up to much higher doses [20].

Thus while the problems with oxide contamination may preclude reaching final conclusions prior to further TEM examinations of cleaner specimens, the overwhelming preponderance of indirect evidence supports the hypothesis that NF efficiently trap and thus manage very high levels of He. The significant implications of these results are profound. In addition to providing excellent corrosion resistance, very high static and creep strength up to high temperatures [21] and good levels of tensile ductility, even after irradiation [22], the results of this study support the hypothesis that NF in NFAs can be used to manage very high levels of He and displacement damage. Of course, the results reported here must be considered preliminary, and many challenges remain.

5. Concluding remarks

In situ He implanter experiments utilizing thin coatings of NiAl deposited on TEM specimen surface have been designed and implemented for the HFIR JP-26, 27 and 28/29 capsules. The first set of post-irradiation characterization studies from JP-26 capsule have been performed on MA957 and Eurofer 97 specimens irradiated to 4–9 dpa and 82–380 appm He at 300–500 °C. The results offer proof in principle of the effectiveness of the in situ He implantation method. The strong evidence that NFs trap He in ultra-small scale bubbles is profoundly significant indicating that further development of high strength NFAs that will enable the development of fusion as a practical future energy source.

Acknowledgements

The authors are grateful to essential theoretical support for He production calculations provided by Dr L.R. Greenwood, US-JAEA program management by Dr R.E. Stoller, technical support for NiAl coating fabrication by Mr D. Klingensmith, Dr H. Kishimoto and Dr M. Alinger, and for irradiation experiments by Mr K. Thoms and Mr D. Heatherly. This research was supported, in part, by the US Department of Energy, Office of Fusion Energy Sciences, under contract DE-FG03-94ER54275 and DE-AC06-76RLO1830 by the US Department of Energy, Office of Nuclear Energy, under contract DE-FC07-05ID14663 and I-NERI 2001-007-F. Research at the ORNL SHaRE Facility was supported in part by the Division of Scientific User Facilities, Office of Basic Energy Sciences, U.S. Department of Energy. ORNL is managed by UT-Battelle, LLC for the U.S. Department of Energy under Contract No. DE-AC05-00OR22725.

References

[1] IFMIF International Team, IFMIF Comprehensive Design Report, 2004.
[2] T. Yamamoto, G.R. Odette, H. Kishimoto, J.-W. Rensman, P. Miao, J. Nucl. Mater. 356 (2006) 27.
[3] Y. Dai, P. Marmy, J. Nucl. Mater. 343 (2005) 247.

[4] J. Henry, X. Averty, Y. Dai, P. Lamagnere, J.P. Pizzanelli, J.J. Espinas, P. Wident, J. Nucl. Mater. 318 (2003) 215.
[5] N.H. Packan, W.A. Coghlan, Nucl. Technol. 40 (1978) 208.
[6] F.A. Garner, Radiat. Eff. 66 (1982) 211.
[7] G.R. Odette, J. Nucl. Mater. 141–143 (1986) 1011.
[8] H. Matsui, K. Nakai, A. Kimura, T. Shikama, M. Narui, H. Kayano, J. Nucl. Mater. 233–237 (1996) 1561.
[9] L.K. Mansur, W.A. Coghlan, ASTM STP 1046 (1989) 315.
[10] L.R. Greenwood, F.A. Garner, B.M. Oliver, M.L. Grossbeck, W.G. Wolfer, ASTM STP 1447 (2004).
[11] M.J. Alinger, G.R. Odette, D.T. Hoelzer, J. Nucl. Mater. 329–333 (2004) 382.
[12] M.J. Alinger, On the formation and stability of nanometer scale precipitates in ferritic alloys during processing and high temperature service, PhD dissertation, University of California, Santa Barbara.
[13] M.K. Miller, D.T. Hoelzer, E.A. Kenik, K.F. Russell, J. Nucl. Mater. 329–333 (2004) 338.
[14] G.R. Odette, T. Yamamoto, H.J. Rathbun, M.Y. He, M.L. Hribernik, J.W. Rensman, J. Nucl. Mater. 323 (2003) 313.
[15] R.J. Kurtz, G.R. Odette, T. Yamamoto, D.S. Gelles, P. Miao, B.M. Oliver, J. Nucl. Mater., in press, doi:10.1016/j.jnucmat.2007.03.121.
[16] M. Rühle, M. Wilkins, Cryst. Latt. Def. 6 (1975) 129.
[17] R.E. Stoller, G.R. Odette, J. Nucl. Mater. 131 (1985) 118.
[18] M. Kilimiankou, R. Lindau, A. Möslang, Micron 36 (2005) 1.
[19] I.-S. Kim, J.D. Hunn, N. Hashimoto, D.L. Larson, P.J. Maziasz, K. Miyahara, E.H. Lee, J. Nucl. Mater. 280 (2000) 264.
[20] B.D. Wirth, T. Yamamoto, G.R. Odette, R.J. Kurtz, F. Gao, H.L. Heinisch, Multiscale modeling of He transport and fate in irradiated nanostructured ferritic alloys, presented in ICFRM-12.
[21] R.L. Klueh, J.P. Shingledecker, R.W. Swindeman, D.T. Hoelzer, J. Nucl. Mater. 341 (2005) 103.
[22] A. Alamo, J.L. Bertin, V.K. Shamardin, P. Wident, J. Nucl. Mater., these Proceedings, doi:10.1016/j.jnucmat.2007.03.166.